IEEE Access
Multidisciplinary | Rapid Review | Open Access Journal

Received October 4, 2021, accepted December 13, 2021, date of publication December 23, 2021, date of current version January 5, 2022.

Digital Object Identifier 10.1109/ACCESS.2021.3138296

Characteristic Mode Analysis Prediction and Guidance of Electromagnetic Coupling Measurements to a UAV Model

MOHAMED Z. M. HAMDALLA[1], (Graduate Student Member, IEEE), BENJAMIN BISSEN[2], (Member, IEEE), JAMES D. HUNTER[3], YUANZHUO LIU[3], (Graduate Student Member, IEEE), VICTOR KHILKEVICH[3], (Member, IEEE), DARYL G. BEETNER[3], (Senior Member, IEEE), ANTHONY N. CARUSO[2], AND AHMED M. HASSAN[1], (Senior Member, IEEE)

[1]Department of Computer Science and Electrical Engineering, University of Missouri—Kansas City, Kansas City, MO 64110, USA
[2]Missouri Institute for Defense & Energy, University of Missouri—Kansas City, Kansas City, MO 64110, USA
[3]Electrical & Computer Engineer Department, Missouri University of Science and Technology, Rolla, MO 65409, USA

Corresponding author: Mohamed Z. M. Hamdalla (mhamdalla@mail.umkc.edu)

This work was supported in part by office of naval research (ONR) under Grant N00014-17-1-2932 and Grant N00014-17-1-3016, and in part by the University of Missouri—Kansas City, School of Graduate Studies Research Award.

ABSTRACT In this work, we study the current coupled to a simplified Unmanned Aerial Vehicle (UAV) model using a dual computational and experimental approach. The simplified surrogate structure reduced the computational burden and facilitated the experimental measurement of the coupled currents. For a practical system, a wide range of simulations and measurements must be performed to analyze the induced current variations with respect to properties of the incident excitation waveform, such as the frequency, angle of incidence, and polarization. To simplify this analysis, Characteristic Mode Analysis (CMA) was used to compute the eigen-currents of the UAV model and predict where and under which RF excitation conditions the coupled current is maximized. We verified these predictions using direct experimental measurement of the coupled currents. The presented simulations and measurements show the usefulness of CMA for studying electromagnetic coupling to practical systems.

INDEX TERMS Electromagnetic coupling, characteristic mode analysis (CMA), electromagnetic interference, current measurement, unmanned aerial vehicles (UAVs).

I. INTRODUCTION

Unmanned aerial vehicles (UAVs) have a wide range of applications and typically operate in congested wireless environments that may cause unwanted interference [1]–[5]. In addition, the commercial UAV industries have recently expressed interest in using UAVs as mobile base stations [6]–[9] and as backhaul infrastructure [6]–[9], which further exacerbate their intra- and inter-induced electromagnetic compatibility (EMC) and electromagnetic interference (EMI) protection and/or shielding requirements.

Currently, it is challenging to model and predict the induced currents in UAV wires and electronics due to electromagnetic interference [10], [11]. Numerous simulations and measurements must be performed for a specific UAV to exhaustively quantify the variations in the coupled currents due to the various flying conditions and possible environments. That is, predicting the coupled current to a UAV is complicated by the variation of its orientation relative to the direction, polarization, and frequency of the incident field. Electromagnetic coupling to practical Devices Under Test (DUTs) shows significant variations, $\sim$ 50 dB or more, with changes in frequency, angle of incidence, polarization, and/or DUT orientation [12]–[15]. Therefore, hundreds and sometimes thousands of measurements are needed to detect the frequency and orientation that causes the maximum electromagnetic coupling to a DUT [12]–[15].

Furthermore, as the DUT gets electrically larger, its radiation characteristics become even more complex, requiring more measurements to detect the frequency and orientation

The associate editor coordinating the review of this manuscript and approving it for publication was Abderrahmane Lakas.

TABLE 1. Comparison between this work and previously reported CMA electromagnetic coupling research.

Reference	Scatterer Complexity	No. Of Modes	Orientation Sensitivity	Experimental Verifications
[27]	Simple (rectangular box)	4	NO	YES
[28]	Simple (rectangular box with slot)	10	NO	NO
[29]	Medium (PCB connected to cable)	3	NO	YES
[30]	Simple (flat circuit loop)	4	NO	NO
	Simple (bent PCB)	6	NO	NO
	Simple (Heatsink model as metallic box)	6	NO	NO
[31]	Simple (High speed connector)	10	NO	NO
[32]	Heatsink	5	NO	YES
[33]	Complex (Car excited by monopole)	10	YES	NO
[34]	Complex (Airplane)	6	YES	YES
[35]	Complex (Airplane)	4	YES	YES
This work	Complex (UAV model)	11	YES	YES

for maximum coupling [14]. Current EMC measurements risk under-testing, where only a limited number of frequencies and orientations are tested, and therefore, the immunity of practical DUTs may be underestimated. On the other hand, measuring an extremely large number of frequencies and orientations, i.e., overtesting, can be unnecessarily expensive and sometimes is practically unrealistic [12]–[15]. ***To avoid undertesting and overtesting in EMC measurements, there is a strong need for a computational tool that can guide experimental measurements by predicting and quantifying the frequency and the orientation that causes the maximum electromagnetic coupling to a complex DUT.***

To meet this need, we adapt the Characteristic Mode Analysis (CMA) to guide experimental measurements by predicting the frequencies and angles of incidence where the electromagnetic coupling is maximum. CMA decomposes the currents induced on a DUT in terms of a set of fundamental independent modes and provides the relative significance of each mode at the frequency of interest [16]. CMA has been extensively employed in the design of antennas and in the analysis of the electromagnetic scattering characteristics of various nanostructures [17]–[20]. Moreover, CMA has been previously employed for studying the use of the frame of a UAV as an antenna [21], [22]. We recently used CMA to study coupling and interference to wires and other simple

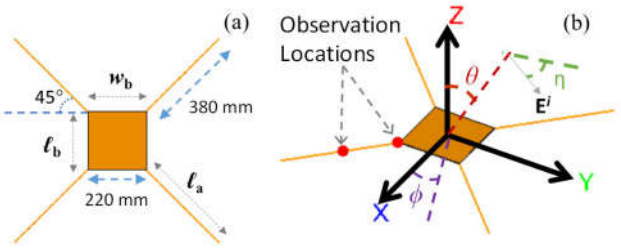

FIGURE 1. (a) A sketch of the quadcopter UAV model showing the general dimensions of the structure, (b) A sketch of the model showing the UAV model orientation with respect to the angles θ, ϕ, and η.

structures [23]–[25]. A preliminary version of this work was presented in [26]. To the best of our knowledge, this is the first *experimentally verified* analysis of coupling and interference to a UAV using CMA. Relevant previously reported CMA studies are summarized in Table 1 and compared to this work.

Most of the papers in Table 1 studied the total radiated power by the DUT. The DUT, therefore, has to be connected to an external source, which is not the goal of this analysis where coupling due to an incident plane wave is the main focus. Ma *et al.* evoked the CMA approach to utilize the characteristic modes of an airplane model to design a direction-finding antenna array operating at the HF band [34]. Wang *et al.* also employed CMA to design a VHF aircraft-integrated antenna array with switchable beams [35]. However, utilizing the aircraft frame as an antenna is not the goal of this analysis. ***The main goal is to avoid under-testing and over-testing by developing a predictive tool that can guide experimental measurements by predicting the frequencies and the angles of incidence that maximize coupling to a UAV.*** In summary, the novel aspects of this work in comparison to the previous studies in Table 1 are: (*i*) A detailed analysis of how CMA can be adapted to guide EMC experiments is presented; (*ii*) a novel UAV quadcopter model is studied; (*iii*) a new experimental setup to verify CMA predictions using a broadband current probe and a Gigahertz Transverse Electromagnetic Cell (GTEM) is developed.

In this paper, a quadcopter UAV and its subsystems are represented by a simplified model that consists of 4 wires attached to a square metallic patch, as shown in Fig. 1. The model was designed to represent the metallic parts typically found in a UAV since the metallic parts dominate the electromagnetic response [36]. Each of the four wires represents the fusion of all the cables commonly found in the arms of a quadcopter, whereas the square metallic patch represents the ground plane of the quadcopter controller. The fusion of the wires with the square metallic patch generates a modal behavior that is significantly different from that of wire or a patch by itself. The UAV model is simple enough to allow the quantitative assessment of the coupled current using both full-wave simulations and experimental measurements. Yet, the model is complex enough to generate conclusions that can be applied to a wide range of quadcopters with similar symmetries in shape.

CMA was applied to calculate the fundamental modes of the proposed UAV model and the characteristics of these modes. Then, we use these modes to predict and explain the coupled current calculated at different locations on the UAV model due to plane wave excitations at different frequencies and incident directions.

This paper is organized as follows. Section II describes the simplified UAV model. Section III summarizes the CMA for the analysis of coupling and interference. Section IV presents the CMA predictions of the currents coupled to the UAV model. Section V presents the sensitivity of the CMA modes to the UAV model dimensions. Section VI describes the developed experimental setup and the validation of the CMA predictions. Finally, Section VII summarizes the conclusions and future work.

II. SIMPLIFIED UAV MODEL

The simplified UAV model is shown in Fig. 1a. The proposed model consists of a square patch with a 220 mm edge length and four wires attached at the patch's corners. The four wires of the model make an angle of 45° with the edge of the square patch. The four identical wires represent the wire connections between the controller and the motors of a quadcopter UAV. The wires' lengths and radii are 380 mm and 0.5 mm, respectively. In UAVs, the wires might have larger radii. Still, we found that the radius of the wire has a negligible effect on the following results as long as the aspect ratio for the wire is high enough to maintain the thin wire configuration. The dimensions of the studied model were chosen to match the frequency range of the current probe used in the measurement setup that will be presented in the next section. But the aspect ratios between the patch and wire lengths match common quadcopters. A perfect electric conductor boundary condition is assigned to all model components in Fig. 1a.

The proposed UAV model was excited by a 150 mV/m incident plane wave at multiple angles of incidence, θ, and ϕ, as defined in Fig. 1b. The polarization angle (η) was fixed at zero in this work due to a limitation in the UAV holder in the experimental setup. However, the effect of the polarization angle will be studied in future work. The magnitude of the excitation signal was chosen to match the value in the experimental setup that will be presented in the next section. The coupling problem studied in this work is linear, so the magnitude of the excitation signal should not affect the CMA predictions.

The coupled current varies with the observation location on the UAV model. To highlight these variations, current monitors were placed at two locations on the UAV model: (i) the edges of one of the four wires, where it meets the corner of the square patch, and (ii) the middle of the wire as shown in Fig. 1b. The two observation locations will be termed corner and middle, respectively, for the remainder of the manuscript.

The UAV model was simulated using the full-wave Method of Moments (MOM) solver FEKO [37]. The simulated coupled currents versus frequency are shown in Fig. 2 for

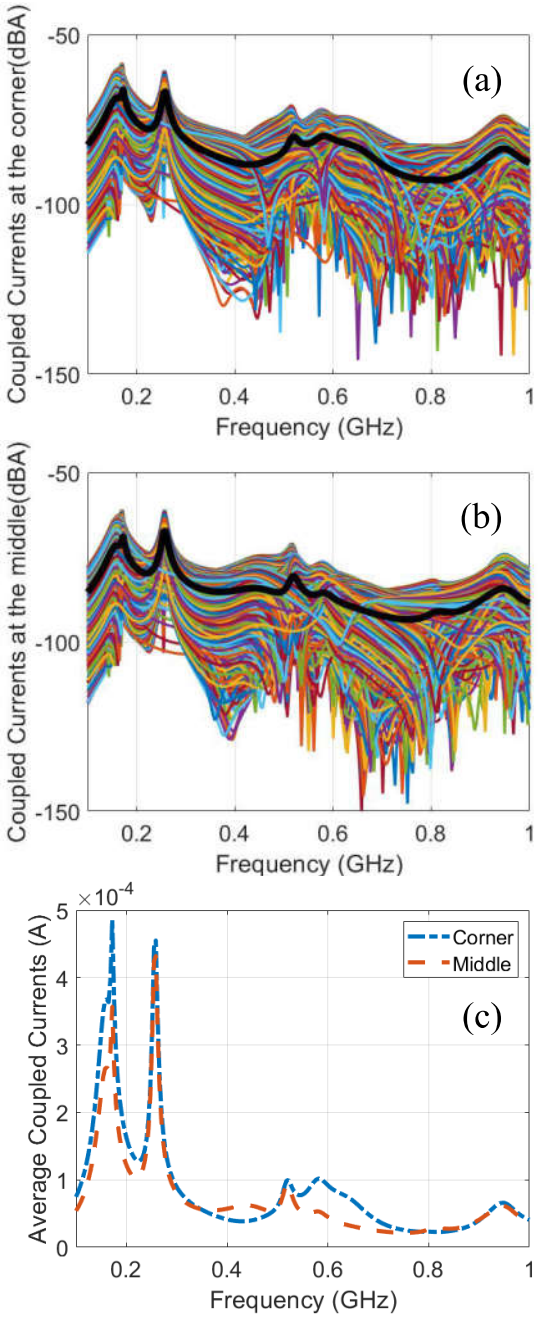

FIGURE 2. The FEKO simulated coupled current to the UAV model at 2701 different angles of incidence θ and ϕ measured at (a) the edge of the wire, and (b) the middle of the wire. (c) The average coupled current over all incidence orientations.

2701 different angles of incidence, θ, and ϕ, where θ varies from 0° to 180° in a 5° step, and ϕ varies from 0° to 360° in a 5° step to cover the entire sphere covering the UAV model. Figure 2a shows the coupled current where the corner of the board meets the wire, and Fig. 2b shows the current at the middle of the same wire. Each colored curve in Fig. 2 represents a different incident direction, i.e., a different $\{\theta, \phi\}$ value. The black curves in Fig. 2a and Fig. 2b represent the average magnitude of the coupled current at each location versus frequency. The coupled current exhibits

significant variations of more than 70 dB depending on the frequency and angle of incidence. The coupled current can even approach zero at some incidence angles, which is not shown in the log-scale curve in Fig. 2a and Fig. 2b. Figure 2c shows the coupled current averaged over all incidence angles at the two observation locations. That is, Fig. 2c shows the black curves in Fig. 2a and Fig. 2b except in linear scale. Clearly, the coupled current differs with respect to the observation location.

From Figure 2, it is difficult to predict the incidence angles that maximize the coupling current or the frequency range where the coupled current is maximum on average. Therefore, the CMA theory is briefly summarized in the following section to show how it can facilitate predicting the coupled current at arbitrary frequencies and incidence angles.

III. CHARACTERISTIC MODE ANALYSIS THEORY

CMA is a full-wave electromagnetic technique that decomposes the total surface current coupled to a DUT into a set of fundamental modes, called eigen-currents, and calculates the relative importance of each mode at any frequency [38]. The modes can be calculated using the following eigenvalue equation [16]:

$$\mathbf{X}\mathbf{J_n} = \lambda_n \mathbf{R}\mathbf{J_n} \tag{1}$$

where $\mathbf{X}$ and $\mathbf{R}$ are the imaginary and real parts of the MOM impedance matrix of the UAV model, respectively; $\mathbf{J_n}$ is the eigen-current, and λ_n is the eigenvalue of mode n. Equation (1) above is solved at every frequency to generate the corresponding $\mathbf{J_n}$ and λ_n values. At any frequency, the total current coupled to a DUT due to an incident field can be expressed as [39]:

$$\mathbf{I} = \sum\nolimits_{n} \frac{V_n \mathbf{J_n}}{(1 + j\lambda_n)} \tag{2}$$

where V_n is the modal excitation coefficient that represents the coupling between the incident fields and mode n. The modal excitation coefficient V_{n} can be calculated using the following integral over the outer surface of the DUT [39]:

$$V_n = \iint \mathbf{J_n}.\mathbf{E^i} ds \tag{3}$$

where $\mathbf{E^i}$ is the incident electric field.

To predict the coupling to any system using CMA, the following parameters should be studied in the following order:

1. Modal significance (MS_n): is independent of the excitation, and it identifies the relative weight of mode n, i.e., it describes the significance of its contribution to the DUT's total coupled current. It can be calculated as: $MS_n = \frac{1}{|1+j\lambda_n|}$. The MS_n has a maximum value of 1, which occurs when the eigenvalue λ_n has a value of zero, and the mode is resonating. At any frequency of interest, the ratio of the values of $\mathrm{MS_n}$ among different modes allows one to identify the modes that dominate the coupled current.
2. Eigen-currents or modal currents $\mathbf{J_n}$: identify the current distribution of each mode n. The modal currents will illustrate the maximum and minimum current locations of each mode.
3. Modal excitation coefficient V_n: represents the coupling between the incident field and mode n of the DUT. The modal excitation coefficient V_n shows which angles of incidence maximize coupling to mode n and which angles of incidence will cause mode n to not be expressed in the total current $\mathbf{I}$.

It is important to re-emphasize that the CMA parameters MS_n and J_n are independent of the incident field. The dependency on the excitation is entirely encapsulated in the modal excitation coefficient V_n. As a result, CMA will give insight into the supported modes of the structure and how to excite each mode without the need to test all possible angles of incidence. Once the MS_n and J_n parameters are calculated, CMA can help guide experimental measurements even if the incident excitation is unknown by identifying the frequencies where the coupling current is maximum. Moreover, CMA will provide the optimum angles of incidence for these modes to be excited, which can reduce the number of frequencies and angles that need to be experimentally measured to accurately quantify the coupling to the UAV, as will be highlighted in the following section.

IV. CMA OF SIMPLIFIED UAV MODEL

Using the full-wave solver FEKO, we performed the CMA of the UAV model in Fig. 1 over the frequency range from 0.1 GHz to 1 GHz. To predict the coupling to the UAV model in Fig. 1 using CMA, the three aforementioned CMA parameters were studied as follows.

A. MODAL SIGNIFICANCE FOR SIMPLIFIED UAV MODEL

The modal significances, MS_n, of the UAV model are shown in Fig. 3. The modal significance spectrum in Fig. 3 shows all the possible coupling pathways to the UAV model. The peaks or the resonance frequencies of the modes represent the frequencies where the coupled current can reach maximum values. For example, Modes 1 and 2 resonate at 0.17 GHz, Mode 3 resonates at 0.19 GHz, and Mode 4 resonates at 0.24 GHz. These are the critical frequencies for the UAV model in Fig. 1 for the frequency range up to 0.4 GHz. The first advantage of the CMA, therefore, is that it identifies the critical coupling frequencies for the DUT. As a result, one can only focus on a few frequencies around where the modes resonate instead of testing the structure at hundreds of frequencies. Table 2 lists the resonance frequencies of the 11 modes in Fig. 3, which determine the frequency regions at which to characterize the UAV.

It is important to emphasize that the coupled current, *for a specific excitation at a particular angle of incidence,* will not show all the peaks in the MS_{n} spectrum in Fig. 3. Different modes are excited at different angles of incidence, as will be described in the following paragraph. However, the MS_n spectrum identifies quantitatively, with no trial and error, the

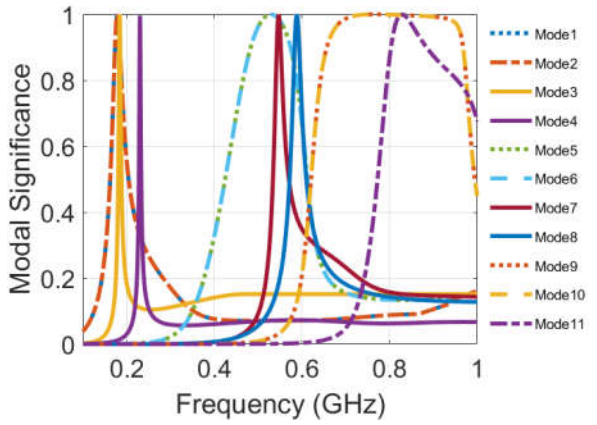

FIGURE 3. Modal significance of the first 11 modes of the proposed UAV model in Fig. 1.

TABLE 2. Resonance frequencies and the optimum incident angles (θ) for the UAV modes.

Mode	Resonance Frequency (GHz)	Optimum Angle of Incidence (θ°)
1	0.17	0
2	0.17	0
3	0.19	90
4	0.24	45
5	0.52	45
6	0.52	60
7	0.55	90
8	0.59	20
9	0.77	0
10	0.77	0
11	0.83	90

critical frequencies, where we need to focus our full-wave simulations and experimental measurements. Moreover, the frequency range where the modes' density is low or where the $MS_{\rm n}$ does not reach high values is the frequency range where the coupled current will be lower on average than other frequency ranges of the same bandwidth. For example, the frequency range between 0.26 GHz and 0.39 GHz does not have any modes with large modal significance. The average coupled current in this frequency range should therefore be lower than that at slightly lower or slightly higher frequencies. This assertion is confirmed in Fig. 2 at all observation locations. In this sense, the observation of MS_n is more useful for identifying where the coupling is *unlikely* to occur rather than where the coupling is *likely* to occur. All the previous conclusions are achieved directly from Fig. 3 without testing hundreds of different angles of incidence.

B. MODAL CURRENTS FOR SIMPLIFIED UAV MODEL

The eigen-current distributions $\mathbf{J_n}$ of the UAV model are shown in Fig. 4. Each eigen-current distribution in Fig. 4 is plotted at the resonance frequency of its mode. The eigen-current distribution in Fig. 4 is normalized with respect to the maximum current value of each mode. The red arrows in Fig. 4 represent the general trend of

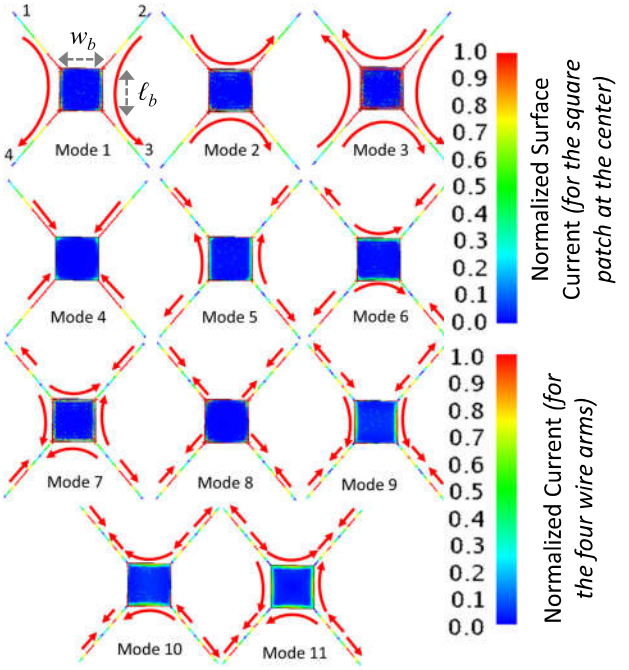

FIGURE 4. Normalized eigen-current distribution of the first 11 modes of the UAV structure. Each eigen-current distribution is plotted at the resonance frequency of its mode.

the current of each mode or eigen-current, whereas the colors show the exact distribution. The hotspots of the modal currents, i.e., the locations where the modal currents are maximum, are shown in red, whereas the locations where the modal currents are zero are shown in blue. For example, Mode 1 has a hotspot at the corner observation location, whereas Mode 9 has a minimum at both the corner and middle observation locations. In general, the modal current is much more important at the corner, as this is generally where the wire connects to the electronic circuitry on-board and where it would be perceived as a noise voltage.

The UAV model in Fig. 1, and many quadcopters, has 4-fold symmetry. This symmetry is reflected in the current distribution of the eigen-currents or modes shown in Fig. 4. For example, Mode 2 is identical to Mode 1 if it is rotated by 90°. Similarly, Mode 5 is identical to Mode 6, and Mode 9 is identical to Mode 10, except for a 90° rotation, as shown in Fig. 4. Due to this symmetry, the three previously mentioned mode pairs have identical $MS_{\rm n}$, as shown in Fig. 3. That is, $MS_1 = MS_2$, $MS_5 = MS_6$, and $MS_9 = MS_{10}$. This means that Mode 1 and Mode 2 will resonate at the same frequency. If the symmetry is broken, then the previous mode pairs will have different modal significance. On the other hand, the current distribution of Mode 3 is a merge of Mode 1 and Mode 2, as shown in Fig. 4, and it resonates at a slightly higher frequency as shown in Fig. 3. This behavior was previously reported in similar but simpler structures that had 4-fold symmetry [40], [41]. However, combining the four wires to the square plate leads to the emergence of new modes

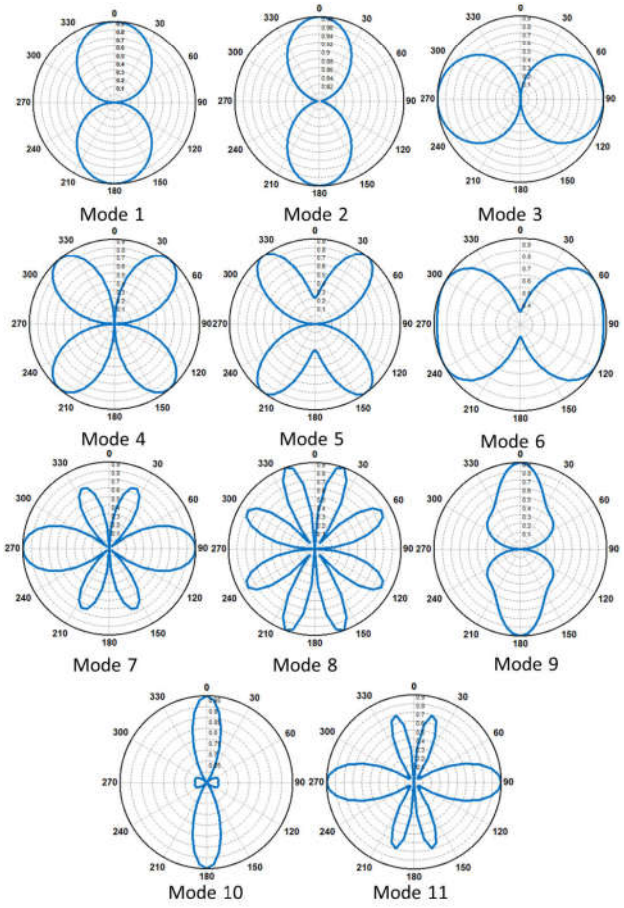

FIGURE 5. Normalized Modal Fields of the first 11 modes of the UAV model. The radiation pattern of each mode is plotted at the resonance frequency of this mode.

that were not easy to predict from the individual modes of the wire or the individual modes of the square plate.

C. MODAL FIELDS/RADIATION PATTERN FOR SIMPLIFIED UAV MODEL

The Modal Excitation Coefficients, $V_{n,}$ can be calculated by using transverse electromagnetic plane waves at different angles of incidence, identifying the incident electric field due to this excitation, $\mathbf{E^i}$, and recalculating the modal excitation coefficient V_n according to (3). The Modal Excitation Coefficients V_n of the first 11 modes, which by reciprocity can be estimated using the radiation characteristics of each mode, calculated using FEKO, are shown in the polar plots in Fig. 5. The radiation pattern of each mode in Fig. 5 is plotted at the resonance frequency of this mode and normalized to its maximum value. All the radiation patterns in Fig. 5 are in the θ plane with a fixed ϕ value of 0° and a fixed polarization angle of 0°. Angles where the modal excitation coefficient is maximum represent the optimum direction to excite a particular mode. Angles of zero modal excitation coefficient in Fig. 5 indicate incident directions that cannot excite the mode regardless of its significance at a particular frequency. For example, Mode 4 cannot be excited at any

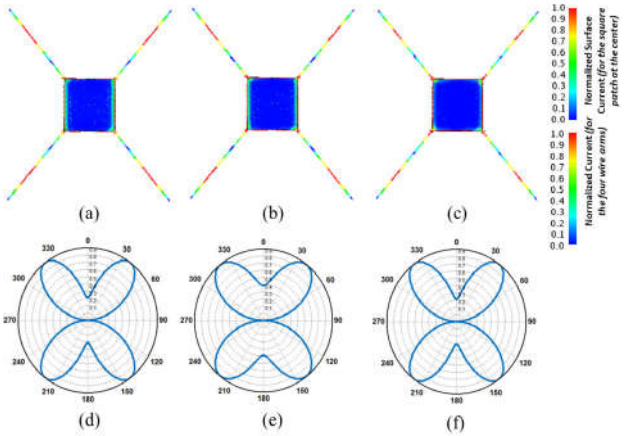

FIGURE 6. Eigen-current distribution of Mode 5 of the UAV structure at: (a) 490 MHz, (b) 520 MHz, (c) 580 MHz. Normalized Modal Fields of Mode 5 of the UAV model at: (d) 490 MHz, (e) 520 MHz, (f) 580 MHz.

frequency at $\theta = 0°$ or at $\theta = 90°$ for $\phi = 0°$, and it can be optimally excited when the incidence angle is at $\theta = 45°$. Table 2 also shows the optimum angles to excite each mode. These angles represent the critical angles of incidence (which can also be related to the DUT orientations) needed to accurately assess the EMC characteristics of the UAV model. As a result, instead of testing thousands of angles as reported in [12], [13], the CMA-generated angles in Table 2 provide a significantly lower number of angles to test and measure the optimum coupling to each mode of the DUT. However, if at one frequency more than one mode is significant, the optimum angle might be in the middle between the angles in Table 2 and can be calculated by analyzing (2).

Most of the 11 modes are narrowband modes. Hence, the changes in the eigen-current distribution of a mode within the frequency band where a mode is significant can be neglected. For example, Fig. 6 presents the eigen-current distribution and the radiation characteristics of Mode 5 at three different frequencies within the bandwidth of Mode 5, i.e, at three frequencies where MS_5 is larger than 0.707. The current distribution of Mode 5 and its radiation pattern does not change dramatically within the bandwidth of the mode. That is, the magnitude of the modal current only changes slightly with frequency, but the hotspot locations are maintained, and the radiation pattern of the modes does not change significantly, as shown in Fig. 6. For frequencies that are significantly larger or smaller than the resonance frequencies of the mode, the eigen-currents and the radiation characteristics of a mode might show significant differences from the patterns at resonance. At these frequencies, however, the MS_n of the modes will be too low to provide any significant contribution to the total coupled current.

D. PREDICTING THE DOMINANT MODE

The CMA information presented in Fig. 3 to Fig. 5 allows us to understand how a wide range of excitations might

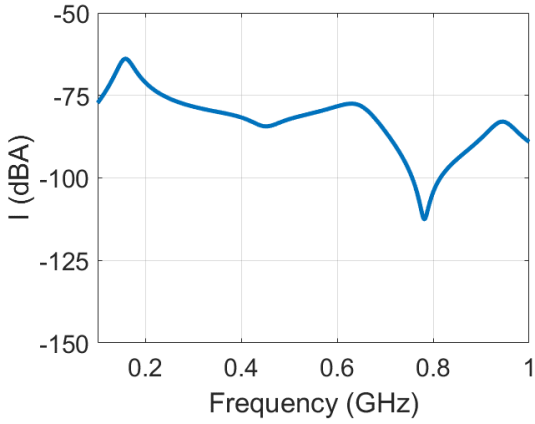

FIGURE 7. Coupled current to the edge of the wire due to an incident wave at $\theta = 0°$.

couple to the UAV. For example, at any frequency of interest, Fig. 3 can identify the significant modes in this frequency range. By investigating Fig. 4, we can determine whether these significant modes have nonzero currents at the location of interest. Next, by examining Fig. 5, we can identify the incident directions that will excite these modes. At these incident directions and in their close vicinity, the coupled current can be maximized. By then performing the summation in (2), we can predict the incident excitation that generates the maximum coupled current.

On the other hand, if the angle of incidence of the excitation is known, we can predict the modes that will be excited. Based on their modal significance in Fig. 3, we can predict the frequencies where coupled current resonates. For example, consider the case where one is interested in the current coupled to the corner observation location when the plane wave excitation is incident at $\theta = 0°$ and $\phi = 0°$. This direction of incidence is only capable of exciting Modes 1, 2, 9, and 10. By examining the current distributions of these modes, shown in Fig. 4, one can see that only Modes 1 and Mode 2 have hotspots, shown in red, at the corner observation location. Modes 9 and 10 have minimal current, shown in blue, at this location. We, therefore, expect the total coupled current to show peaks only at the resonance frequencies of Modes 1 and 2, shown to be around 0.17 GHz in Fig. 3. Figure 7 confirms these predictions by showing the full-wave simulated current at the corner observation location due to a plane wave excitation at $\theta = 0°$. A clear peak is present in the coupled current in Fig. 7 near the frequency of 0.17 GHz, which is the same resonance frequency of Modes 1 and 2. Figure 7 also shows a strong minimum near 0.77 GHz. This minimum is not due to the absence of current coupling pathways because Modes 9, 10, and 11 are significant at this frequency. The minimum in the coupled current at 0.77 GHz exists because these 3 modes contribute zero current at the corner observation location. All of these predictions were achieved from the CMA information generated in Fig. 3 to Fig. 5. The following section describes how varying the UAV model dimensions can affect the modal behavior previously described.

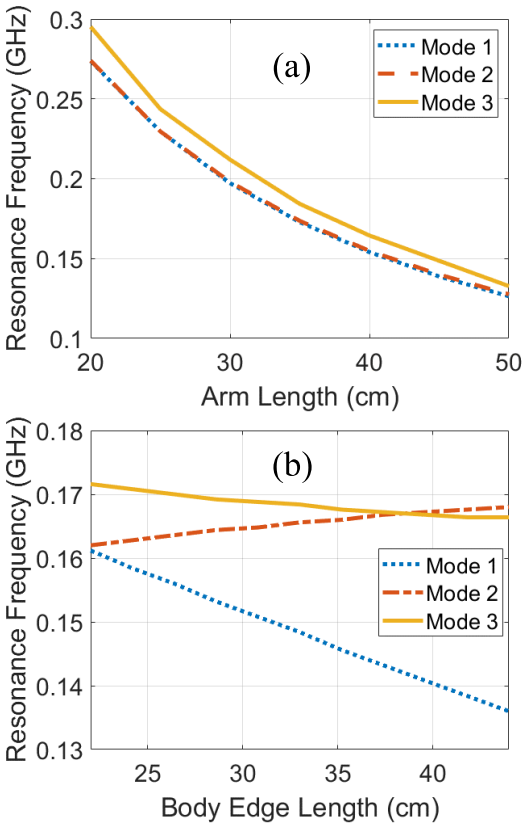

FIGURE 8. The resonance frequencies of the modal significance of Modes 1-3 when (a) the arm length ℓa was varied and (b) when the body length ℓb was varied.

V. SENSITIVITY OF MODES TO UAV MODEL DIMENSIONS

In this section, we explore how the modal characteristics vary with the dimensions of the UAV model. Three dimensions of the UAV model in Fig. 1a were varied: ℓ_a (arm length), ℓ_b (length of the controller board), and w_b (width of the controller board). The effect of varying the UAV's arm length ℓ_a on the modal behavior for fixed center body dimensions $\ell_b = w_b = 220$ mm, is plotted in Fig. 8a. For this analysis, the arm length ℓ_a was increased from 200 mm to 500 mm in 50 mm increments. For each value of ℓ_a, the modal significance, MS_n, was recalculated (not shown for brevity), and the resonance frequency of MS_1 –MS_3 was plotted as shown in Fig, 8a. Fig. 8a shows that the resonance frequencies of Modes 1-3 decrease proportional to $\sim 1/\ell_a$.

The effect of varying the patch's length, ℓ_b, for a fixed arm length and patch width, $\ell_a = 380$ mm and $w_b = 220$ mm, is shown in Fig. 8b. As the body length ℓ_b increases from 220 mm to 440 mm in 22 mm increments, the center patch becomes a rectangle instead of a square breaking the 4-fold symmetry. Instead of Mode 1 and Mode 2 showing identical resonance frequencies, Fig. 8b shows that as ℓ_b is increased that Mode 1 and Mode 2 start showing opposite trends. That is, the resonance frequency of Mode 1 starts to decrease, and the resonance frequency of Mode 2 starts to increase. The resonance frequency of Mode 1 is the most sensitive to the change in ℓ_b, decreasing from 0.162 GHz to

0.136 GHz, which corresponds to a 15.5% reduction in the resonance frequency for a 100% increase in ℓ_b. On the other hand, Mode 2 only shows a 3.5 % increase in its resonance frequency for a 100 % increase ℓ_b.

The current distribution of the modes shown in Fig. 4 explains this behavior because the current distribution of Mode 1 is parallel to ℓ_b, but the current distribution of Mode 2 is parallel to w_b. Therefore, increasing ℓ_b and keeping w_b constant has a marginal effect on Mode 2 but significantly affects Mode 1. Mode 3 is a hybrid mode combining the current distributions of Mode 1 and Mode 2, as shown in Fig. 4. Its resonance frequency follows approximately the average of the trends of Mode 1 and Mode 2. Since Mode 1 shows a more significant decrease than Mode 2, the overall trend of Mode 3 is to decrease with an increase in ℓ_b.

The effect of varying the UAV size was also studied. Sadraey *et al.* classified the UAV according to their sizes, where the size is defined as the longest dimension of the UAV [42]. For a quadcopter, then, the size of the UAV is measured from the opposite corner motors. Most commercial off-the-shelf (COTS) UAVs fall within the following four classes: Micro UAVs where the size is less than 10 cm, Mini UAVs where the size is between 10 cm and 30 cm, Very Small UAVs when the size is between 30 cm and 50 cm, and Small UAVs where the size is from 50 cm up to 2 m. Since the model in Fig. 1 is classified as a Small UAV, its dimensions were scaled down to cover other UAV classes and to study the effect of the UAV size on the modes of the frame. Figure 9 illustrates the variation of the resonance frequencies of Mode 1, Mode 3, and Mode 4 when the overall size of the UAV changes. The analysis of the resonance frequency of Mode 2 is omitted since it is identical to Mode 1 for the symmetric model, as illustrated in the previous section. Figure 9 shows that the resonance frequencies of the modes scale up when the size of the UAV scales down in a logarithmic fashion. Thus, the coupling problem studied in this work is invariant with respect to simultaneous change of the dimensions and frequencies, and therefore, the CMA analysis performed in this work can be scaled based on the size of the UAV frame. Moreover, Fig. 9 shows the frequency range of the first four modes for different UAV size classes. For example, the resonance frequencies of the first four modes of UAVs in the "Mini" class should be confined between 0.6 GHz and 3 GHz if they are similar in shape to the model in Fig. 1.

In summary, the advantage of the CMA is that it explicitly delineates the current distribution of the modes. This current distribution will allow us to predict which modes will change their resonance frequencies and which modes will have their resonance frequencies unaffected by a change in the DUT's geometry. The mode resonances are directly related to the coupled current, which is a weighted summation of the modes as in (2). Moreover, scaling the overall size of the UAV leads to a linear shift in the resonance. Now that the modal characteristics and behavior are fully quantified, the next section shows how CMA can be used to predict the coupled current in experimental measurements.

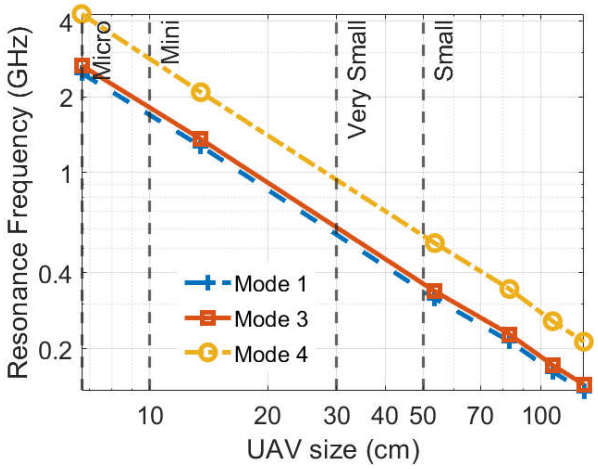

FIGURE 9. The resonance frequencies of the modal significance of Modes 1,3, and 4 when the size of the UAV was varied according to the size of different UAV classes.

VI. EXPERIMENTAL TESTING OF CMA PREDICTIONS

An EMCO 5317 GTEM was used for testing the CMA predictions. The GTEM cell has a maximum septum height of 1.5 m and a recommended frequency range of DC - 18 GHz. At its feed, the GTEM has a 50 Ω 7/16 DIN coaxial input. Port 1 of a Rohde & Schwarz ZVA 24 vector network analyzer (VNA) was connected to this feed to generate the incident TEM wave. The GTEM was terminated with pyramidal foam absorbers and distributed resistive loads to prevent any reflections. The UAV model in Fig. 1 was built from copper wires and a square copper sheet. It was placed inside the GTEM at a 1.5 m septum height to be excited by the generated TEM fields, as shown in Fig. 10. The field strength at the UAV location can be estimated by dividing the input voltage at the TEM-cell port by the septum height. A 225 mV stimulation was applied at port 1 of the GTEM, giving a field strength at the UAV location of ∼225/1.5 = 150 mV/m. A BCP-512 clamp-on broadband current probe with an operable frequency range of 1 MHz – 1 GHz was placed at different locations on the UAV model to sample the total coupled current. The experimental setup in Fig. 10 was used to validate the CMA predictions since the total coupled current is a weighted summation of the modes in Figs. 3-5. The current probe was connected to Port 2 of the VNA. The measured S-parameter, S_{21}, was converted to the coupled current through the following formula [43], [44]:

$$\left|I_{\text{probe}}\right|_{\text{dBA}} = |V_G|_{\text{dBV}} + |s_{21}|_{\text{dB}} - \text{cable loss}_{\text{dB}} - |Z_T|_{dB\Omega} \quad (4)$$

where V_G is the voltage at the GTEM input port and is calculated based on the required field strength at the location of the UAV. The summation of the V_G and s_{21} yields the voltage received at the current probe. Z_T is the probe transfer impedance, which represents the transfer

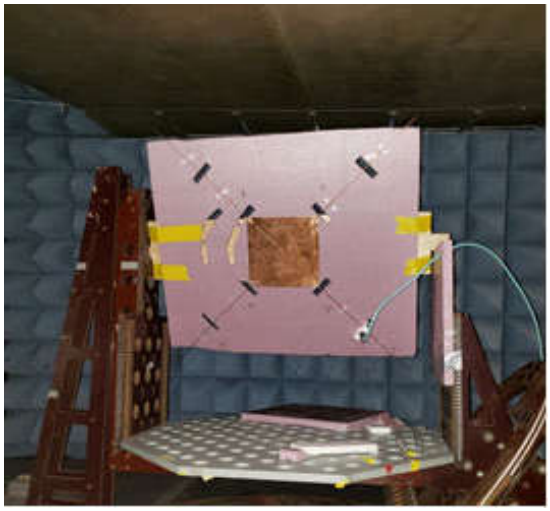

FIGURE 10. Experimental setup showing the realized UAV model inside the GTEM and the current probe at one location.

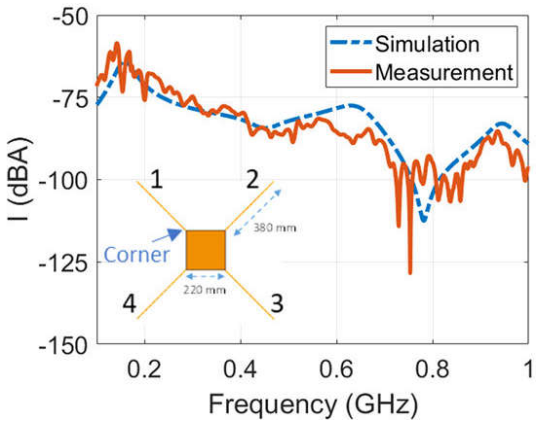

FIGURE 11. Comparison between the measured and simulated currents at the edge of Wire 1 for normal incidence $\theta = 0°$ and $\phi = 0°$.

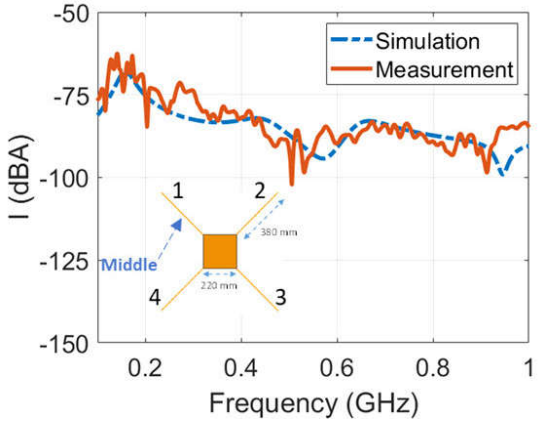

FIGURE 12. Comparison between the measured and simulated currents at the middle of Wire 1 for normal incidence $\theta = 0°$ and $\phi = 0°$.

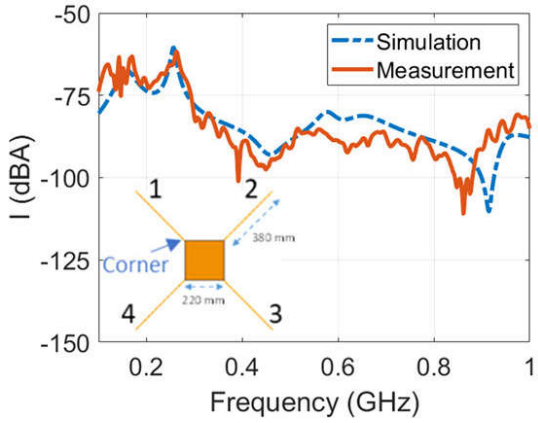

FIGURE 13. Comparison between the measured and simulated currents at the edge of Wire 1 for oblique incidence $\theta = 45°$ and $\phi = 0°$.

function that converts the voltage readings from the current probe into corresponding current values, as obtained from the datasheet of the current probe [43]. The "*Cable Loss*" term represents the attenuation the measured signal experiences as it travels from the current probe to the VNA and can be measured experimentally. Z_T and the "*Cable Loss*" are typically negative when represented in decibels. Experimental measurements will focus on the frequencies and incident angles summarized in Table 2 since CMA predicts that these frequencies will maximize the coupled current.

In the first experimental measurement, the UAV model was oriented normal to the incident wave inside the GTEM, i.e., at $\theta = 0°$ and $\phi = 0°$ and with the polarization angle at zero. The current probe was placed at the corner location, and the coupled current was measured and compared to the simulations that used incident plane waves with an electric field amplitude of 150 mV/m. Excellent agreement was achieved between the measurements and the simulations, as shown in Fig. 11. For both the simulated and the measured current, the peak current was achieved near 0.17 GHz, the resonance frequency of Modes 1 and 2 as shown in Table 2.

A minimum was experimentally observed in the coupled current near 0.77 GHz, even though this is the resonance frequency of Modes 9 and 10, as shown in Table 2. Figure 4 shows that these modes' current distributions have a minimum at the corner location. The maximum of their current distribution occurs at the middle location. Therefore, CMA predicts that this dip in the coupled current will disappear if the current probe is moved to the middle of the wire. Figure 12 shows the simulated and the measured current at the middle of the wire for the same UAV orientation. The dip in the coupled current near 0.77 GHz is significantly reduced, validating the CMA prediction. Specifically, in Fig. 11, the minimum coupled current was less than -115 dBA, but in Fig. 12, it was on the order of $\sim$ - 90 dBA.

To further examine CMA's ability to predict coupled current, we examined Mode 4, which cannot be excited by normal incidence. Figure 5 and Table 2 show that the optimum angle to excite Mode 4 is $\theta = 45°$. Therefore, if we change the orientation of the incident wave relative to the

UAV model, Mode 4 can be excited. We expect a new peak to emerge in the coupled current at its resonance frequency of 0.24 GHz, as shown in Fig. 3. Figure 13 shows the coupled current at the corner location at an oblique incidence angle of $\theta = 45°$ and $\phi = 0°$ and polarization angle of zero. As predicted by CMA, a new peak emerges at 0.24 GHz caused primarily by Mode 4. CMA, therefore, provides a straightforward technique, without thousands of trials and error, to predict the frequencies and angles of incidence where the peaks in the coupled current exist.

VII. CONCLUSION

In this work, we developed a simple model for the wires and electronic circuitry of quadcopter Unmanned Aerial Vehicles (UAVs) using a square metallic patch and four wires. Characteristic Mode Analysis (CMA) was successfully applied to calculate the fundamental modes supported by the UAV model and the characteristics of these modes. The knowledge of this modal behavior facilitates the quantification of the UAV's electromagnetic susceptibility to external interference and allows one to identify the resonant frequencies that maximize the coupled current. Moreover, we showed that the CMA could predict the orientations that maximize the coupled current to the UAV model at a particular frequency. Inspite of the relative simplicity of the UAV model, its predictions showed qualitative agreement with the true response of quadcopters. The CMA predictions were tested experimentally by building the UAV model, exciting it with plane waves inside a GTEM, and measuring the coupled current using a clamp-on current probe. Excellent agreement was achieved between the simulations and the measurements validating this approach for quantifying electromagnetic coupling and interference to UAVs and similar devices of interest. The CMA could efficiently predict the incident angles, frequencies, and probe locations where the coupled current to the UAV model will be maximum. Thus CMA could guide the EMC testing of a practical DUT by reducing the number of necessary experimental measurements needed to make sure that maximum coupling is detected. In the future, we will extend the CMA approach employed herein to study more complicated and practical UAV models with a larger number of wires and electronics and by expanding the model from a quasi-3D to a full 3D model.

REFERENCES

[1] *Drones are About to Fill the Skies Within the Next 5 Years*, BI Intelligence, IEyeNews, Cayman Islands.

[2] P. Zhan, D. W. Casbeer, and A. L. Swindlehurst, "A centralized control algorithm for target tracking with UAVs," in *Proc. 39th Asilomar Conf. Signals, Syst. Comput.*, Oct. 2005, pp. 1148–1152, doi: 10.1109/ACSSC.2005.1599940.

[3] J. R. Insua, S. A. Utsumi, and B. Basso, "Estimation of spatial and temporal variability of pasture growth and digestibility in grazing rotations coupling unmanned aerial vehicle (UAV) with crop simulation models," *PLoS ONE*, vol. 14, no. 3, Mar. 2019, Art. no. e0212773, doi: 10.1371/journal.pone.0212773.

[4] J. Kim and J. P. Hespanha, "Cooperative radar jamming for groups of unmanned air vehicles," in *Proc. 43rd IEEE Conf. Decis. Control (CDC*, vol. 1, Dec. 2004, pp. 632–637, doi: 10.1109/CDC.2004.1428715.

[5] D. W. Casbeer, S.-M. Li, R. W. Beard, R. K. Mehra, and T. W. McLain, "Forest fire monitoring with multiple small UAVs," in *Proc., Amer. Control Conf.*, vol. 5, Jun. 2005, pp. 3530–3535, doi: 10.1109/ACC.2005.1470520.

[6] Z. Xiao, P. Xia, and X.-G. Xia, "Enabling UAV cellular with millimeter-wave communication: Potentials and approaches," *IEEE Commun. Mag.*, vol. 54, no. 5, pp. 66–73, May 2016, doi: 10.1109/MCOM.2016.7470937.

[7] M. Mozaffari, W. Saad, M. Bennis, and M. Debbah, "Unmanned aerial vehicle with underlaid device-to-device communications: Performance and tradeoffs," *IEEE Trans. Wireless Commun.*, vol. 15, no. 6, pp. 3949–3963, Jun. 2016, doi: 10.1109/TWC.2016.2531652.

[8] C. Zhan, Y. Zeng, and R. Zhang, "Energy-efficient data collection in UAV enabled wireless sensor network," *IEEE Wireless Commun. Lett.*, vol. 7, no. 3, pp. 328–331, Jun. 2018, doi: 10.1109/LWC.2017.2776922.

[9] J. Lyu, Y. Zeng, R. Zhang, and T. J. Lim, "Placement optimization of UAV-mounted mobile base stations," *IEEE Commun. Lett.*, vol. 21, no. 3, pp. 604–607, Mar. 2017, doi: 10.1109/LCOMM.2016.2633248.

[10] T. Li, B. Wen, Y. Tian, Z. Li, and S. Wang, "Numerical simulation and experimental analysis of small drone rotor blade polarimetry based on RCS and micro-Doppler signature," *IEEE Antennas Wireless Propag. Lett.*, vol. 18, no. 1, pp. 187–191, Jan. 2019, doi: 10.1109/LAWP.2018.2885373.

[11] A. V. Khristenko, M. O. Konovalenko, M. E. Rovkin, V. A. Khlusov, A. V. Marchenko, A. A. Sutulin, and N. D. Malyutin, "Magnitude and spectrum of electromagnetic wave scattered by small quadcopter in *X*-band," *IEEE Trans. Antennas Propag.*, vol. 66, no. 4, pp. 1977–1984, Apr. 2018, doi: 10.1109/TAP.2018.2800640.

[12] L. Jansson and M. Backstrom, "Directivity of equipment and its effect on testing in mode-stirred and anechoic chamber," in *Proc. IEEE Int. Symp. Electromagn. Compatability. Symp. Rec.*, vol. 1, Aug. 1999, pp. 17–22, doi: 10.1109/ISEMC.1999.812860.

[13] M. Hoijer and V. Isovic, "Frequency resolved susceptibility testing as a substitute for angular resolved susceptibility testing," in *Proc. Int. Symp. Electromagn. Compat.*, vol. 1, Aug. 2004, pp. 29–34, doi: 10.1109/ISEMC.2004.1349991.

[14] *Electromagnetic Compatibility (EMC)—Part 4-3: Testing and Measurement Techniques—Radiated, Radio Frequency, Electromagnetic Field Immunity Test*, document EN 61000-4-3, Sep. 2020. [Online]. Available: https://webstore.iec.ch/publication/59849

[15] S. Kim, Y.-H. Noh, J. Lee, J. Lee, J.-S. Choi, and J.-G. Yook, "Electromagnetic signature of a quadcopter drone and its relationship with coupling mechanisms," *IEEE Access*, vol. 7, pp. 174764–174773, 2019, doi: 10.1109/ACCESS.2019.2956499.

[16] R. F. Harrington and J. R. Mautz, "Theory of characteristic modes for conducting bodies," *IEEE Trans. Antennas Propag.*, vol. AP-19, no. 5, pp. 622–628, Sep. 1971, doi: 10.1109/TAP.1971.1139999.

[17] M. Cabedo-Fabres, E. Antonino-Daviu, A. Valero-Nogueira, and M. F. Batalle, "The theory of characteristic modes revisited: A contribution to the design of antennas for modern applications," *IEEE Antennas Propag. Mag.*, vol. 49, no. 5, pp. 52–68, Oct. 2007, doi: 10.1109/MAP.2007.4395295.

[18] S. Dey, D. Chatterjee, E. J. Garboczi, and A. M. Hassan, "Plasmonic nanoantenna optimization using characteristic mode analysis," *IEEE Trans. Antennas Propag.*, vol. 68, no. 1, pp. 43–53, Jan. 2020, doi: 10.1109/TAP.2019.2938705.

[19] K. C. Durbhakula, A. M. Hassan, F. Vargas-Lara, D. Chatterjee, M. Gaffar, J. F. Douglas, and E. J. Garboczi, "Electromagnetic scattering from individual crumpled graphene flakes: A characteristic modes approach," *IEEE Trans. Antennas Propag.*, vol. 65, no. 11, pp. 6035–6047, Nov. 2017, doi: 10.1109/TAP.2017.2752218.

[20] A. M. Hassan, F. Vargas-Lara, J. F. Douglas, and E. J. Garboczi, "Electromagnetic resonances of individual single-walled carbon nanotubes with realistic shapes: A characteristic modes approach," *IEEE Trans. Antennas Propag.*, vol. 64, no. 7, pp. 2743–2757, Jul. 2016, doi: 10.1109/TAP.2016.2526046.

[21] Y. Chen and C.-F. Wang, "Electrically small UAV antenna design using characteristic modes," *IEEE Trans. Antennas Propag.*, vol. 62, no. 2, pp. 535–545, Feb. 2014, doi: 10.1109/TAP.2013.2289999.

[22] S.-M. Sow, L. Guo, S.-G. Zhou, and T.-H. Chio, "Electrically small structural antenna design for small UAV based on characteristics modes," in *Proc. 11th Eur. Conf. Antennas Propag. (EUCAP)*, Mar. 2017, pp. 2134–2138, doi: 10.23919/EuCAP.2017.7928206.

[23] M. Z. M. Hamdalla, A. N. Caruso, and A. M. Hassan, "Predicting electromagnetic interference to a terminated wire using characteristic mode analysis," in *Proc. Int. Appl. Comput. Electromagn. Soc. Symp. (ACES)*, Jul. 2020, pp. 1–2, doi: 10.23919/ACES49320.2020.9196133.
[24] M. Z. M. Hamdalla, A. M. Hassan, and A. N. Caruso, "Characteristic mode analysis of the effect of the UAV frame material on coupling and interference," in *Proc. IEEE Int. Symp. Antennas Propag., USNC-URSI Radio Sci. Meeting*, Jul. 2019, pp. 1497–1498, doi: 10.1109/APUSNCURSINRSM.2019.8888344.
[25] M. Z. M. Hamdalla, B. B. Bissen, A. N. Caruso, and A. M. Hassan, "Experimental validations of characteristic mode analysis predictions using GTEM measurements," in *Proc. IEEE Int. Symp. Antennas Propag. North Amer. Radio Sci. Meeting*, Jul. 2020, pp. 1799–1800, doi: 10.1109/IEEECONF35879.2020.9330415.
[26] M. Z. M. Hamdalla, A. M. Hassan, A. Caruso, J. D. Hunter, Y. Liu, V. Khilkevich, and D. G. Beetner, "Electromagnetic interference of unmanned aerial vehicles: A characteristic mode analysis approach," in *Proc. IEEE Int. Symp. Antennas Propag., USNC-URSI Radio Sci. Meeting*, Jul. 2019, pp. 553–554, doi: 10.1109/APUSNCURSINRSM.2019.8888398.
[27] F. A. Dicandia, S. Genovesi, and A. Monorchio, "Efficient excitation of characteristic modes for radiation pattern control by using a novel balanced inductive coupling element," *IEEE Trans. Antennas Propag.*, vol. 66, no. 3, pp. 1102–1113, Mar. 2018, doi: 10.1109/TAP.2018.2790046.
[28] S. Ghosal, A. De, A. P. Duffy, and A. Chakrabarty, "Selection of dominant characteristic modes," *IEEE Trans. Electromagn. Compat.*, vol. 62, no. 2, pp. 451–460, Apr. 2020, doi: 10.1109/TEMC.2019.2909932.
[29] Y. S. Cao, Y. Wang, L. Jiang, A. E. Ruehli, J. Fan, and J. L. Drewniak, "Quantifying EMI: A methodology for determining and quantifying radiation for practical design guidelines," *IEEE Trans. Electromagn. Compat.*, vol. 59, no. 5, pp. 1424–1432, Oct. 2017, doi: 10.1109/TEMC.2017.2677199.
[30] Q. Wu, H.-D. Bruns, and C. Schuster, "Characteristic mode analysis of radiating structures in digital systems," *IEEE Electromagn. Compat. Mag.*, vol. 5, no. 4, pp. 56–63, 4th Quart., 2016, doi: 10.1109/MEMC.2016.7866235.
[31] X. Wang, Y. S. Cao, L. Jiang, A. E. Ruehli, S. He, H. Zhao, J. Hu, J. Fan, and J. L. Drewniak, "Investigation of the radiation mechanism for high-speed connectors," in *Proc. IEEE 26th Conf. Electr. Perform. Electron. Packag. Syst. (EPEPS)*, Oct. 2017, pp. 1–3, doi: 10.1109/EPEPS.2017.8329711.
[32] X. Yang, Y. S. Cao, X. Wang, L. Zhang, S. He, H. Zhao, J. Hu, L. Jiang, A. Ruehli, J. Fan, and J. L. Drewniak, "EMI radiation mitigation for heatsinks using characteristic mode analysis," in *Proc. IEEE Symp. Electromagn. Compat., Signal Integrity Power Integrity (EMC, SI PI)*, Jul. 2018, pp. 374–378, doi: 10.1109/EMCSI.2018.8495291.
[33] Y. S. Cao, M. Ouyang, Y. Wang, and J. Fan, "EMI modeling for antenna-chassis system using characteristic mode analysis," in *Proc. IEEE Symp. Electromagn. Compat., Signal Integrity Power Integrity (EMC, SI PI)*, Jul. 2018, pp. 181–186, doi: 10.1109/EMCSI.2018.8495389.
[34] R. Ma and N. Behdad, "Design of platform-based HF direction-finding antennas using the characteristic mode theory," *IEEE Trans. Antennas Propag.*, vol. 67, no. 3, pp. 1417–1427, Mar. 2019, doi: 10.1109/TAP.2018.2884878.
[35] C. Wang, Y. Chen, G. Liu, and S. Yang, "Aircraft-integrated VHF band antenna array designs using characteristic modes," *IEEE Trans. Antennas Propag.*, vol. 68, no. 11, pp. 7358–7369, Nov. 2020, doi: 10.1109/TAP.2020.2997468.
[36] J. Hunter, Y. Liu, D. Floyd, A. Hassan, V. Khilkevich, and D. Beetner, "Characterization of the electromagnetic coupling to UAVs," presented at the Annu. Directed Energy Sci. Technol. Symp., Mar. 2018.
[37] *Simulation for Connectivity, Compatibility, and Radar | Altair Feko*. Accessed: Oct. 23, 2021. [Online]. Available: https://www.altair.com/feko/
[38] S. Huang, J. Pan, C.-F. Wang, Y. Luo, and D. Yang, "Unified implementation and cross-validation of the integral equation-based formulations for the characteristic modes of dielectric bodies," *IEEE Access*, vol. 8, pp. 5655–5666, 2020, doi: 10.1109/ACCESS.2019.2963278.
[39] Y. Chang and R. F. Harrington, "A surface formulation for characteristic modes of material bodies," *IEEE Trans. Antennas Propag.*, vol. AP-25, no. 6, pp. 789–795, Nov. 1977, doi: 10.1109/TAP.1977.1141685.
[40] R. J. Garbacz and E. H. Newman, "Characteristic modes of a symmetric wire cross," *IEEE Trans. Antennas Propag.*, vol. AP-28, no. 5, pp. 712–715, Sep. 1980, doi: 10.1109/TAP.1980.1142388.
[41] N. Peitzmeier and D. Manteuffel, "Upper bounds and design guidelines for realizing uncorrelated ports on multimode antennas based on symmetry analysis of characteristic modes," *IEEE Trans. Antennas Propag.*, vol. 67, no. 6, pp. 3902–3914, Jun. 2019, doi: 10.1109/TAP.2019.2905718.
[42] M. Sadraey, "Unmanned aircraft design: A review of fundamentals," *Synth. Lect. Mech. Eng.*, vol. 1, no. 2, p. i-193, Sep. 2017, doi: 10.2200/S00789ED1V01Y201707MEC004.
[43] *A.H. Systems Broadband Current Probe Series Operation Manual*. Accessed: Sep. 9, 2021. [Online]. Available: https://www.atecorp.com/atecorp/media/pdfs/data-sheets/ah-systems-bcp-500-series_manual.pdf
[44] C. R. Paul, *Introduction to Electromagnetic Compatibility*. Hoboken, NJ, USA: Wiley, 2006.

MOHAMED Z. M. HAMDALLA (Graduate Student Member, IEEE) received the B.Sc. and M.Sc. degrees in electronics and communications engineering from Arab Academy for Science, Technology and Maritime Transport, Alexandria, Egypt, in 2012 and 2016, respectively. He is currently pursuing the Ph.D. degree in electrical engineering with the University of Missouri—Kansas City, USA. His current research interests include antennas, metamaterials, microwave filters, electromagnetic compatibility and interference, characteristic mode theory, and applications.

BENJAMIN (BEAR) BISSEN (Member, IEEE) received the B.A. degree in political science from the University of Illinois—Urbana Champaign, in 2018, and the M.S. degree in physics from the University of Missouri—Kansas City, in 2020, where he is currently pursuing the Ph.D. degree in physics. His current research interests include electromagnetic compatibility, automation, and sensor integration.

JAMES D. HUNTER received the B.Sc. degree in electrical engineering from the Missouri University of Science and Technology (formerly the University of Missouri—Rolla), Rolla, MO, USA, in 2017, where he is currently pursuing the Ph.D. degree in electrical engineering. He is a GAANN Fellowship Recipient and a Research Assistant with the S&T EMC Laboratory. His current research interests include electromagnetic compatibility and interference, RF measurements and simulations, and statistical characterization of electromagnetic coupling to electronic devices.

YUANZHUO LIU (Graduate Student Member, IEEE) received the B.E. degree in electrical and computer engineering from the Huazhong University of Science and Technology, Wuhan, China, in 2017, and the M.S. degree in electrical engineering from the Missouri University of Science and Technology (formerly the University of Missouri—Rolla), Rolla, MO, USA, in 2019, where she is currently pursuing the Ph.D. degree in electrical engineering with the EMC Laboratory. Her research interests include electromagnetic interference, radio frequency desense, signal integrity, noise, and jitter analysis in high-speed digital systems.

VICTOR KHILKEVICH (Member, IEEE) received the Ph.D. degree in electrical engineering from the Moscow Power Engineering Institute, Technical University, Moscow, Russia, in 2001. He is currently an Associate Research Professor with the Missouri University of Science and Technology, Rolla, MO, USA. His research interests include microwave imaging, automotive electromagnetic compatibility modeling, and high-frequency measurement techniques.

DARYL G. BEETNER (Senior Member, IEEE) received the B.S. degree in electrical engineering from Southern Illinois University, Edwardsville, IL, USA, in 1990, and the M.S. and D.Sc. degrees in electrical engineering from Washington University, St. Louis, MO, USA, in 1994 and 1997, respectively.

He is currently a Professor in electrical and computer engineering with the Missouri University of Science and Technology, Rolla, MO, USA (Missouri S&T), is the Former Chair of the Missouri S&T ECE Department, is the Director of the Missouri S&T Electromagnetic Compatibility Laboratory and is the Director of the Center for Electromagnetic Compatibility, a National Science Foundation Industry/University Cooperative Research Center. He has authored more than 150 research papers, two book chapters, and multiple patents/invention disclosures, and received several best paper awards or nominations. His research interests include a wide variety of topics including electromagnetic immunity and emissions from the integrated circuit to the system level. He was a recipient of the IEEE EMC Society Technical Achievement Award, in August 2020, and was the IEEE-HKN C. Holmes MacDonald Outstanding Young Electrical Engineering Professor, in 2003. He has served the IEEE EMC Society as the University Grants Committee Chair, the SC-5 Special Committee on Power Electronics Secretary, the Educational Committee Secretary and the Vice-Chair, the Tutorials Chair, and as the TC-4 Electromagnetic Interference Control Secretary and served IEEE as an Associate Editor for the IEEE TRANSACTIONS ON INSTRUMENTATION AND MEASUREMENT and as the Chair for the IEEE Medal for Environmental and Safety Technologies Selection Committee. He is the Former Chair of the Central States ECE Department Heads Association.

ANTHONY N. CARUSO received the B.A. degree in mathematics, physics and philosophy from the Bethany College, Lindsborg, KS, USA, in 2000, and the M.S. and Ph.D. degrees in physics & astronomy from the University of Nebraska—Lincoln, Lincoln, NE, USA, in 2003 and 2004, respectively. From 2004 to 2006, he was a Staff Scientist with the Center for Nanoscale Science and Engineering, North Dakota State University, Fargo, ND, USA, before starting with the University of Missouri—Kansas City as an Assistant Professor in physics, in 2007, where he is currently a Curators' Professor in physics and electrical engineering. His current interests include finding new ways to store and release electrical energy as impulses through clever semiconductor and inductive structures and mechanisms to hack plant physiology coupled with high efficiency energy recycling.

AHMED M. HASSAN (Senior Member, IEEE) received the B.Sc. degree (Hons.) in electronics and communications engineering and the M.Sc. degree in electronics and communications engineering from Cairo University, Giza, Egypt, in 2004 and 2006, respectively, and the Ph.D. degree in electrical engineering from the University of Arkansas, Fayetteville, AR, USA, in 2010.

From 2011 to 2012, he was a Postdoctoral Researcher with the Department of Electrical Engineering, University of Arkansas. From 2012 to 2015, he was a Postdoctoral Researcher with the National Institute of Standards and Technology, Gaithersburg, MD, USA. He joined the University of Missouri—Kansas City, in 2015, where he is currently an Associate Professor and the Director of the Multidisciplinary Multiscale Electromagnetics Laboratory (MMEL), Computer Science Electrical Engineering Department. His current research interests include the broad field of applied electromagnetics including areas, such as nanoelectromagnetics, bioelectromagnetics, electromagnetic compatibility and interference, nondestructive evaluation (NDE), and experimental microwaves/terahertz imaging.

Dr. Hassan was a recipient of the 2018 University of Missour—Kansas City Chancellor's Early Career Award for Excellence in Teaching, the 2014 Outstanding Poster Award in the 21st Annual NIST Sigma Xi Postdoctoral Poster Presentation, and the 2007 Doctoral Academy Fellowship at the University of Arkansas.